Calibration Status and Results for Wide Field Camera 3

Randy A. Kimble

NASA, Goddard Space Flight Center, Greenbelt, MD 20771

and the WFC3 Team

Abstract.   Wide Field Camera 3 (WFC3) is a general-purpose imager in development for installation in HST Servicing Mission 4 (SM4). Covering the wavelength range of 200-1700 nm in two observing channels, WFC3 offers powerful new capabilities, particularly in the near-ultraviolet and near-infrared bands. During 2004, the instrument was integrated and underwent a substantial suite of end-to-end characterization and performance tests. In this paper, we present a brief overview of the design and scientific purpose of WFC3, summarize the results of its test program to date, and highlight some recent developments in detector technology that will further enhance the performance of WFC3's IR channel.

1.   Design and Purpose of WFC3

The WFC3 program originated in 1997 when NASA decided that the target date for the end of the HST mission would be moved from 2005 to 2010. Recognizing that this date would place HST's complement of imagers beyond their nominal design lifetimes, the HST Project initiated the development of a new camera to ensure and extend HST's imaging capabilities into those later years. WFC3 was thus conceived, to be developed as a facility instrument on behalf of the astronomical community (that is, with no PI team and no Guaranteed Time Observations). Day-to-day scientific guidance is provided by a Science Integrated Product Team from NASA/GSFC and STScI, with broad guidance exercised by a community-based Science Oversight Committee, chaired by R. O'Connell of the University of Virginia.

As problems with NASA's shuttle program have delayed the planned SM4 until at least late 2007 (with end-of-mission in $\approx$2013), the need for a backup camera for HST has, if anything, increased, but WFC3 provides much more than imaging "insurance" for Hubble. WFC3 is a powerful scientific imager in its own right, offering unique capabilities and scientific potential, particularly in the near-ultraviolet (NUV) and near-infrared (NIR) bands (very nicely complementary to the *I*-band-optimized Advanced Camera for Surveys).

WFC3 features two channels. The UV/Visible (UVIS) channel covers 200-1000 nm and is based on a two-CCD mosaic (4096$\times$4096 total pixels). The CCDs are low-noise, UV-enhanced devices manufactured by e2v (formerly Marconi), yielding an unprecedented combination of sensitivity and field of view for NUV imaging with HST. The UVIS channel offers a 160$\times$160 arcsec field with 0.039 arcsec pixels, with a rich assortment of broad, medium, and narrowband filters and a UV grism.

The IR channel (800-1700 nm) incorporates a custom HgCdTe focal plane array (FPA), developed by Rockwell Scientific Company, with 1014$\times$1014 imaging pixels. The novel 1700 nm cutoff of this array permits low-dark-current operation at temperatures that can be reached with WFC3's passive radiator and thermo-electric cooling, and minimizes the impact of thermal background radiation from the relatively warm HST environment. The IR channel covers a field of 139$\times$123 arcsec at $\approx$0.130 arcsec sampling, also with a sizable
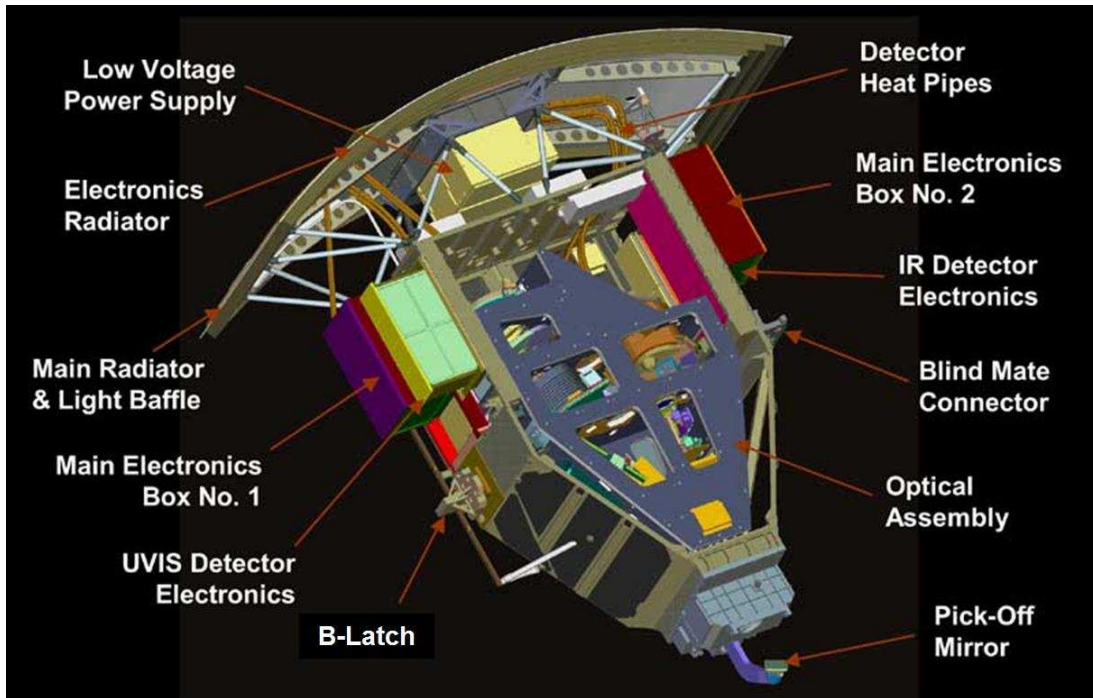
Figure 1: Schematic diagram of WFC3. Significant elements (radiator, enclosure, UVIS filter mechanism) are re-used WF/PC-1 hardware, while the electronics have substantial heritage from STIS, NICMOS, and ACS.
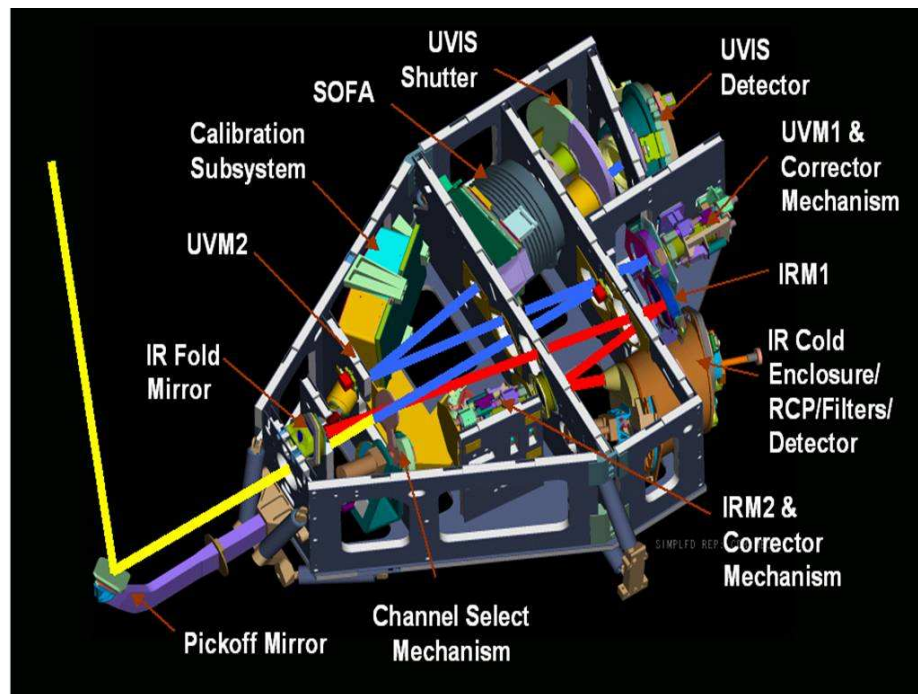

Figure 2: Optical layout of WFC3. The WFC3 pickoff mirror captures the on-axis beam from HST, which is then directed (as the shaded light beams in the figure indicate) to either the UVIS or IR channel, depending on the position of the Channel Select Mechanism.
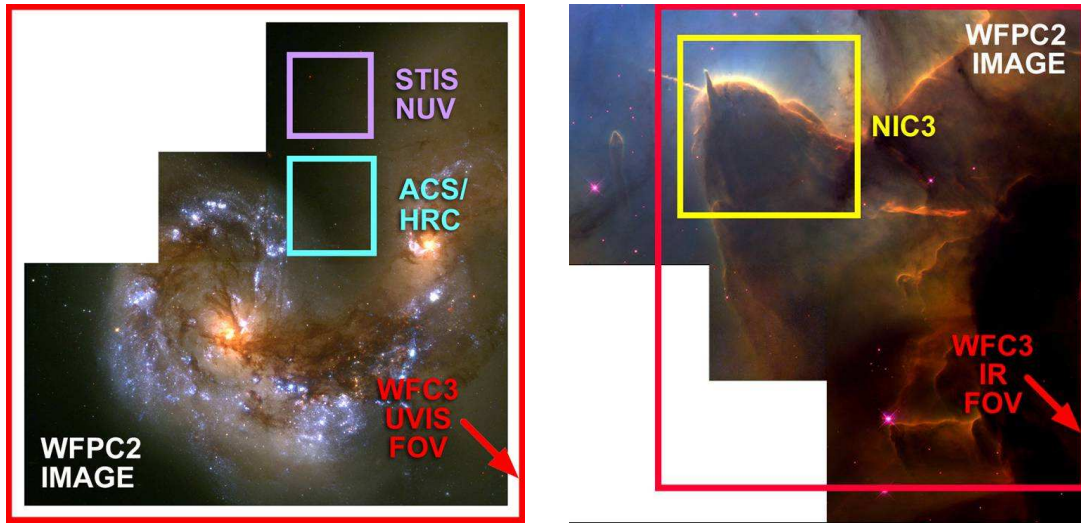
Figure 3: Schematic diagrams of the field of view (FOV) of the WFC3 UVIS (left) and IR (right) channels, compared with the FOV of current HST instruments. Note the large size of the UVIS FOV compared with those of the other HST imagers offering high NUV sensitivity (the STIS NUV and ACS HRC channels) and the dramatic increase in IR FOV vs. the largest field NICMOS camera.

complement of filters and grisms. The improved detector sensitivity and dramatic increase in field of view vs. NICMOS result in a major advance in NIR imaging for HST.

WFC3 is intended for installation into the radial instrument bay currently occupied by WFPC2 (see Figures 1 and 2 for schematic diagrams of the instrument's configuration). The dramatic advances in field of view (FOV) offered by WFC3 for NUV and NIR imaging are shown schematically in Figure 3. Coupling the FOV increases with the high sensitivity of the instrument at these wavelengths, WFC3 will enable a rich program of scientific observations. The UVIS channel will be particularly well suited to the study of the star formation history in nearby galaxies (by virtue of the high sensitivity of NUV observations to the age of stellar populations) and the chemical enrichment history of galaxies, and to the search for Ly α dropouts in the problematic redshift range of $z = 1 - 2$. The NUV portion of the UVIS bandpass will also probe one of the darkest spectral regions of the natural sky background, permitting the detection of very low surface brightness objects.

The IR channel will take advantage of the dark IR sky in space to study: Type Ia supernovae and the accelerating universe, galaxy formation at high redshifts, and the sources of cosmic re-ionization. The penetrating power of IR observations will be brought to bear on the dust-enshrouded processes of star formation, and the IR channel will also enable new studies of water and ices in our own solar system.

In short, WFC3 is a powerful new instrument, offering unique capabilities for astronomical observing. See Kimble, MacKenty, & O'Connell (2004) for additional details regarding the WFC3 design and scientific potential.

2. Highlights of Ambient and Thermal-Vacuum Testing

As is well known, there was a period throughout 2004 during which SM4 was officially cancelled on the grounds of shuttle safety. Currently, as directed by the NASA Administrator, the HST program is back to working toward a shuttle-based SM4, nominally scheduled for December 2007; a formal decision to execute the mission will not be made, however, until successful return-to-flight for the shuttle program.
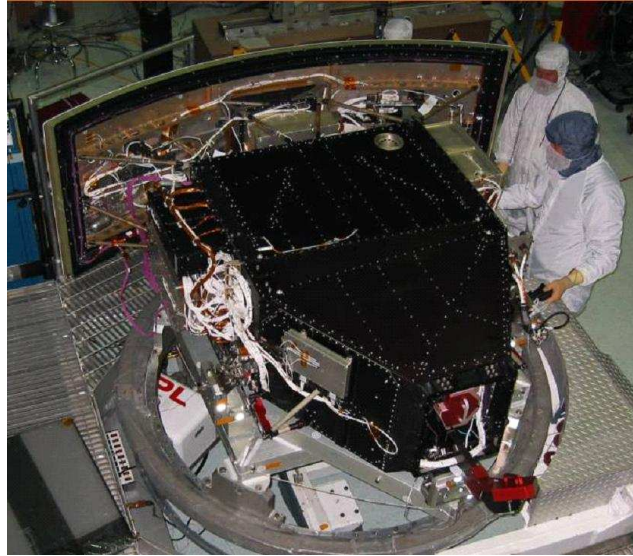
Figure 4: Photo of WFC3, integrated in preparation for its thermal-vacuum performance characterization test in late 2004.

Fortunately, the WFC3 program was not directed to stop work during 2004. Instead, the team was permitted to continue integration of the instrument (see Figure 4) toward execution of a "performance demonstration" thermal-vacuum test (with the idea that after demonstration of the capabilities of WFC3, it could potentially be made available for a non-HST launch opportunity). Though this meant that some issues that would normally be dealt with during instrument integration were deferred (and added to a "lien list" to be resolved now that the program has returned to a prepare-for-flight status), it enabled WFC3 to carry out an early and invaluable end-to-end evaluation of the instrument's performance.

The performance characterization thermal-vacuum test was carried out in August-October 2004 (with significant ambient testing of the UVIS channel performed before that time). Though the goals of the tests were not to produce a full scientific calibration, all aspects of WFC3 were investigated, with very satisfactory results overall. We highlight some of the key results here, in Tables 1 and 2 and Figures 5-8; additional details regarding the thermal-vacuum test program are presented by Bushouse et al. (2006) in this volume.

Table 1: Key UVIS Channel Thermal-Vacuum Results.

Characteristic	Specification; Goal	Measured
Dark current	<20 e$^-$/pix/hour	0.2-0.4 e$^-$/pix/hour
Read noise (rms)	<4 e$^-$/pix; <3 e$^-$/pix	2.98-3.08 e$^-$/pix
Linearity	$<5\%$ deviation over 100-50,000 e$^-$	$<3\%$ deviation
Encircled energy	250nm: >0.75; >0.80 in 0$''$20 633nm: >0.75; >0.80 in 0$''$25	250nm: 0.78-0.81 633nm: 0.77-0.81
Cal system	10,000 e$^-$/pix in <10 min Uniform to $<2\times$	<1 min $\approx 7\times$
Filter ghosts	$<0.2\%$ of incident in a ghost	up to 15% for a small subset of filters (see text)

Table 2: Key IR Channel Thermal-Vacuum Results.

Characteristic	CEI spec; goal	Measured
Dark current	<0.4 e$^-$/pix/s; <0.1 e$^-$/pix/s	0.1 e$^-$/pix/s
Read noise (rms) (CDS pair of images)	<15 e$^-$/pix; <10 e$^-$/pix	≈ 23 e$^-$/pix
Full well	$>100,000$ e$^-$/pix; $>150,000$ e$^-$/pix	$\approx 100,000$ e$^-$/pix
Encircled energy (1000nm)	>0.56; >0.61 in $0\farcs25$ >0.72; >0.80 in $0\farcs37$	0.52-0.56^a 0.73-0.77
Encircled energy (1600nm)	>0.48; >0.54 in $0\farcs25$ >0.75; >0.80 in $0\farcs60$	0.40-0.44^a 0.77-0.81
Cal system	$10,000$ e$^-$/pix in <10 min Uniform to $<2\times$	<1 min $\approx 25\times$
Filter ghosts	$<0.2\%$ of incident in a ghost	$<0.2\%$

[a]The measured encircled energies require small corrections for the difference in central obscuration between the ground test aberrated beam simulator vs. the real HST Optical Telescope Assembly; with those corrections, the measured encircled energies are in line with the requirements (see Figure 5).

The detector performance in end-to-end thermal-vacuum testing summarized in Tables 1 and 2 is in complete agreement with the results of testing at the device and sub-system level: the UVIS CCDs show a low read noise of $3\,\mathrm{e}^-$ rms (the lowest of any HST CCD camera) and negligible dark current; the IR detectors were known to have higher-than-specified read noise, but the very low dark current vs. specifications and the measured throughput of the optical system bring the overall sensitivity of the channel within specification.

Optical performance is excellent (Figure 5), with many encircled energy results well exceeding specifications; slight departures seen in the IR channel are likely the result of a small amount of detector interpixel diffusion.

The throughput of the UVIS channel is in close agreement with pre-test predictions (based on individual component measurements) throughout the visible, and (delightfully) well exceeds those predictions in the NUV range, where our early CCD calibrations had underestimated the sensitivity of the UV-enhanced devices (the NUV test setup has since been improved). In the IR, the end-to-end throughput runs systematically 10-15% below component-based predictions across the band. This discrepancy is a bit beyond the expected error bars in the comparison, so the team is investigating to see whether there is a correctable source for the discrepancy. In any case, the measured end-to-end throughput in thermal-vacuum testing confirms the dramatic discovery potential for WFC3 in both the NUV and NIR bands; see Figure 8 for a tantalizing comparison of WFC3 vs. other HST instruments.

The most noteworthy performance discrepancies shown in the tables are the severe ghosting exhibited by a small subset of the UVIS filter set and poor performance of the internal calibration subsystem at this stage of integration. The filter ghosting issue is described in detail by Baggett et al. (2006) in this volume; to summarize briefly, we have procured greatly improved replacements for all high-priority filters with out-of-spec ghost intensities. The Scientific Oversight Committee has confirmed the acceptability of these replacements and the replacement process is in work. For the calibration subsystem, the UVIS channel simply requires improved alignment, while the IR channel flat-field non-uniformity will be rectified by replacing one of the transfer lenses in the calibration path.

Overall the thermal-vacuum characterization program was extremely successful and provides invaluable guidance in the team's ongoing preparation of the instrument for flight.

WFC3 UVIS PSF Encircled Energy   UVN01

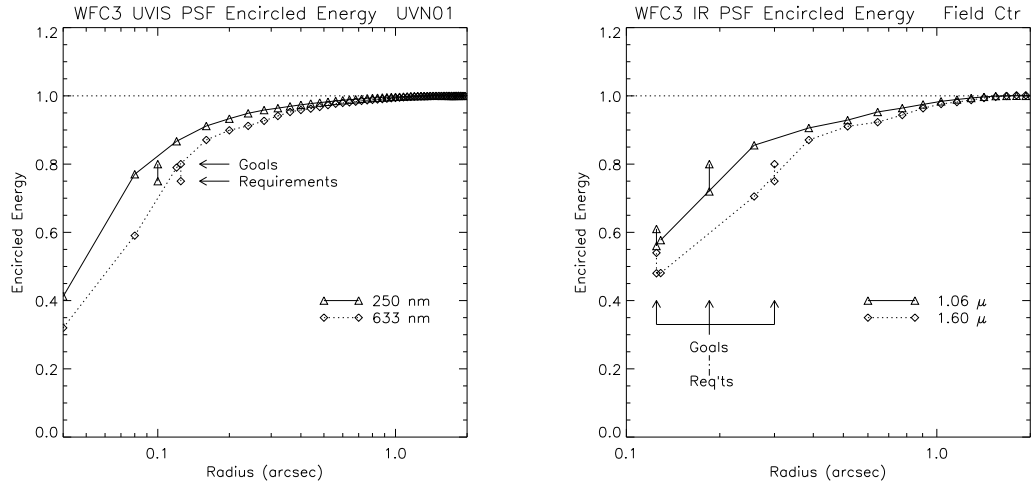WFC3 IR PSF Encircled Energy   Field Ctr

Figure 5: (left) Encircled energy vs. radius for UVIS channel images. (right) Encircled energy vs. radius for IR channel images. Phase-retrieval measurements of the delivered wavefront confirm the high quality of the optical system. Encircled energy results in the IR channel are likely affected by a small amount of interpixel diffusion in the detector.
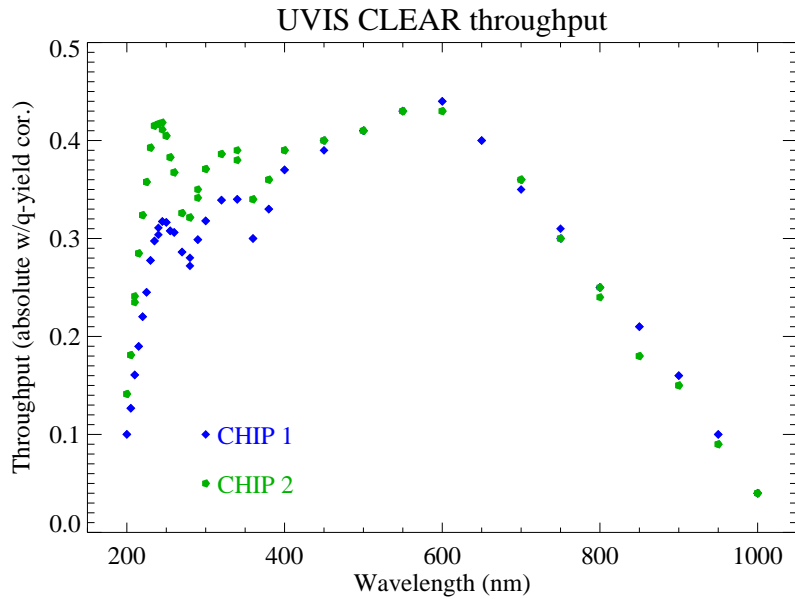
UVIS CLEAR throughput

Figure 6: Unfiltered throughput (detected photons/input photons) for the UVIS channel; representative values are shown for each of the CCDs. The actual signal detected at short wavelengths (in electrons/input photon) is higher than shown here due to CCD quantum yield, which exceeds one electron per detected photon below ≈340nm. The curves shown here have been corrected for that effect.
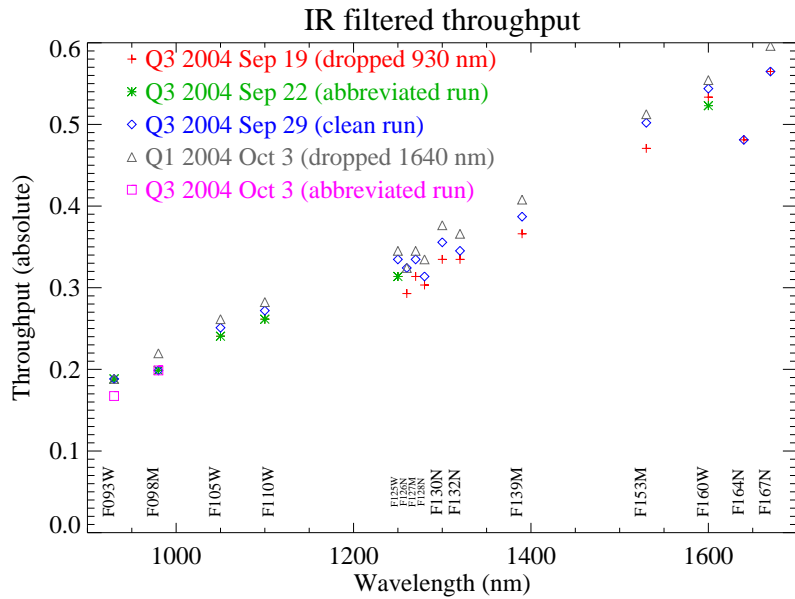
Figure 7: Throughput of IR channel as measured in thermal-vacuum test, including filters. The overall slope vs. wavelength is dominated by the detector quantum efficiency.
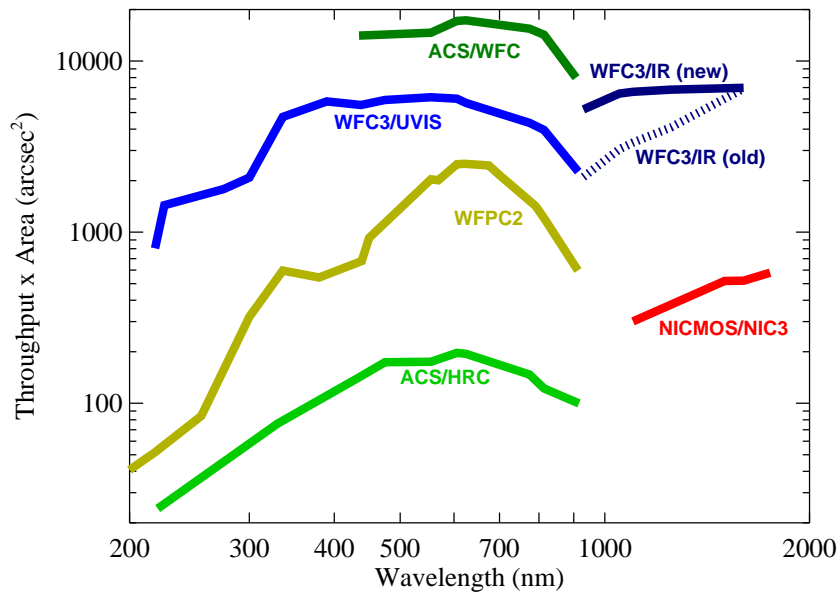

Figure 8: Comparative discovery efficiencies of various HST imagers. The discovery efficiency is defined as the throughput of the instrument (detected photons/input photons) × the area of the instrument's field of view. The curves are generated by calculating this quantity, including the filter transmission, at the center of band for the different broadband filters available for each instrument. For the WFC3/IR channel, the dashed curve (old) is based on the end-to-end throughput measured in the thermal-vacuum testing described above; the solid curve (new) scales up the throughput to the higher quantum efficiencies offered by new IR detectors that are currently in fabrication for flight (see Section 3). WFC3's uniquely powerful capabilities in the NUV and NIR bands are evident.

3.   Improved Detectors for the IR Channel

In the course of development of WFC3, radiation testing of the IR detector arrays revealed an unexpected phenomenon. When exposed to a high-energy proton beam in the ground radiation test, the detector images showed a significant diffuse signal between the direct proton hits (Figure 9 - left). Further testing isolated the source of the diffuse signal to the thick CdZnTe substrate on which the HgCdTe detection layer is grown (Waczynski et al. 2005); when hit by high-energy particles, the substrate appears to produce luminescent output that is then detected by the HgCdTe layer.

Without a detailed understanding of the physical mechanism, scaling from the laboratory test conditions to the orbital radiation environment, and from one FPA to another, is uncertain. Our best estimate, however, is that the background produced in orbit by cosmic rays from this effect could be comparable to the intrinsic dark current of the devices, thus lowering the faint-target sensitivity of the IR channel if the effect is not eliminated.

Fortunately, in the time since our current flight FPA was acquired, Rockwell Scientific Company has successfully developed a process for removing the CdZnTe substrate after hybridizing the HgCdTe arrays. WFC3 radiation tests confirm that substrate removal completely eliminates the radiation-induced background phenomenon (Figure 9 - right). Hence, substrate-removed lots of WFC3 IR arrays are currently being procured, with the intention of packaging a new FPA for flight and removing the radiation risk.

Of even greater benefit, the substrate-removed FPAs show extremely high quantum efficiency (QE) across the WFC3 IR band, greatly improved over the performance of the current WFC3 flight device, FPA64 (Figure 10). (FPA64 was in the instrument for the thermal-vacuum testing described above.) The performance observed for the new devices appears to cluster in two groups: one with relatively flat QE across the WFC3 IR band, and one with more sloped QE, but both offering marked improvement over FPA64.

The new devices do have one drawback. So far, the substrate-removed devices produced for WFC3 exhibit higher dark current tails than seen in FPA64 (Figure 11). Interestingly, there is a clear correlation that the group of detectors with high, flat QE curves shows systematically larger dark current tails than the lower QE group.

Additional cooling of the detector produces marked dark current benefits. Our thermal-vacuum test demonstrated good thermal performance margin, so we can confidently project that the IR FPA can be operated at least down to 145K vs. the previous operating point of 150K. This 5 degree shift drops the dark current by more than a factor of two and significantly reduces the fraction of pixels in the dark current tail (Figure 12).

Fabrication of additional devices from the substrate-removed lots is ongoing, and Rockwell believes that small adjustments in the substrate-removal process for the remaining parts will yield better combinations of QE and dark current performance. However, we demonstrate below that even the currently available devices offer markedly improved scientific performance for WFC3 vs. FPA64, even neglecting that detector's radiation vulnerability.

In Table 3, we show a metric of "survey speed" in different filter bands, for several candidate WFC3 detectors (cf. Robberto et al. 2005). This metric is defined as the product of the speed (i.e. 1/exposure time required) to reach a given faint target magnitude in the given filter band × the area of the IR channel's field of view. The metric is then normalized so that the value for the NIC3 camera of NICMOS (the widest field imager of that instrument) is equal to 1.

The metric is tabulated for the *J* & *H* bands (F110W and F160W, respectively) and a representative narrow-band filter (F126N). The values for FPA64 demonstrate the order-of-magnitude increase in survey speed over NICMOS previously touted for the WFC3 IR channel (with our measured end-to-end throughputs). For each of the devices, we tabulate the mean dark rate for a particular percentage of the pixels, and we then scale the effective FOV for WFC3 by that percentage to account for the effects on surveying efficiency of masking the hot pixel tails.
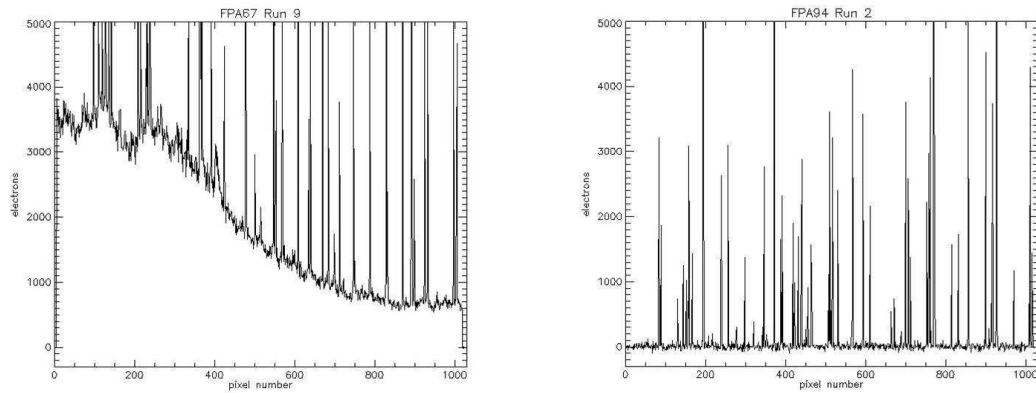
Figure 9: Radiation test results for WFC3 IR detectors. (left) cut across irradiated image for FPA with CdZnTe substrate, showing diffuse signal between the discrete hits; (right) analogous image cut for substrate-removed FPA, showing elimination of luminescence effect.
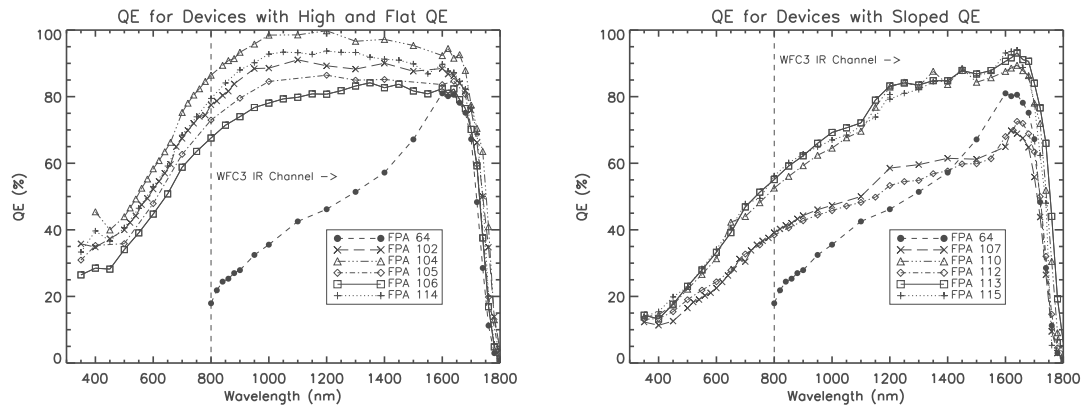

Figure 10: (left) Strikingly high QEs for group of substrate-removed IR FPAs, compared with QE of current flight detector, FPA 64. (right) QEs of other group of substrate-removed FPAs; less QE improvement, but better dark current performance than devices at left.
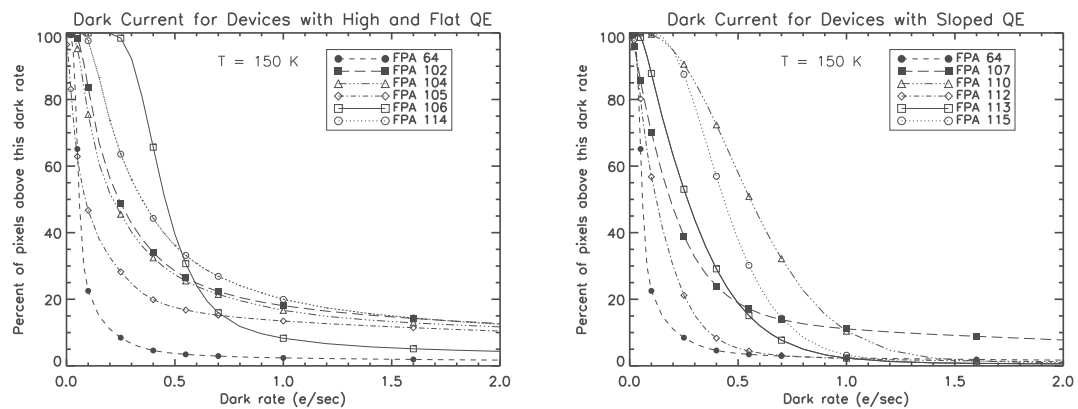

Figure 11: Cumulative dark current histograms for the two groups of detectors and current flight device, FPA64. At each value of dark current, the quantity plotted is the percentage of pixels with dark current exceeding that value. The group of substrate-removed devices with higher QE also exhibits a higher percentage of pixels in a high dark current tail.
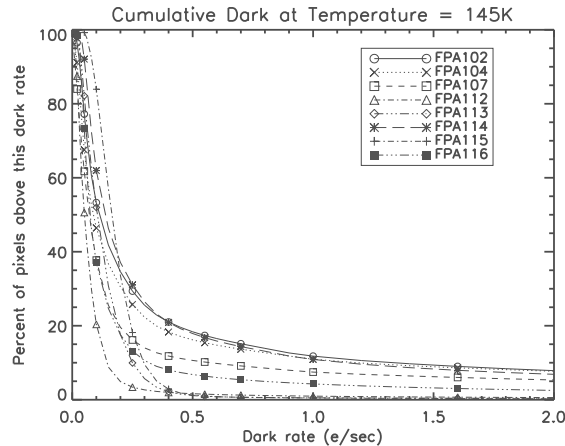
Figure 12: Cumulative Dark Current Histograms at 145K Operating Temperature

The results show that even a conservative choice of substrate-removed detector, such as FPA112 or FPA116 (with little or no hot pixel masking required), offers noticeable performance benefits over FPA64. The best high-QE parts (FPAs 104 and 105) offer more dramatically improved survey efficiency, though with greater complexity in observing (more dithering) and calibration to deal with the higher hot pixel percentages. Finally, the last line of the table shows the superb performance of a detector offering an "ideal" combination of parameters: 90% QE across the band along with low dark tail and read noise.

Table 3: Survey Speed Metric for Candidate IR Detectors.

Detector	CDS Noise	Mean Dark (145K)	F110W	F160W	F126N
FPA64	24	0.04 (100%)	12.5	9.1	11.7
FPA112	24	0.09 (100%)	15.6	7.7	12.4
FPA116	29	0.18 (98%)	20.0	7.4	13.0
FPA104	33	0.14 (90%)	28.7	10.4	18.2
FPA105	28	0.10 (90%)	26.6	10.0	20.6
Potential FPA?	20	0.04 (100%)	31.4	12.5	36.1

In conclusion, WFC3 will be a scientifically powerful addition to the HST suite of instruments. The WFC3 team looks forward to completing the instrument and providing this new capability to the astronomical community.

References

Baggett, S. et al., 2006, The 2005 *HST Calibration Workshop*. Eds. A. M. Koekemoer, P. Goudfrooij, & L. L. Dressel, this volume, 348

Bushouse, H. et al.,2006, The 2005 *HST Calibration Workshop*. Eds. A. M. Koekemoer, P. Goudfrooij, & L. L. Dressel, this volume, 343

Kimble, R. A., MacKenty, J. W., & O'Connell, R. W. 2004, Proc. SPIE, 5487, 266

Robberto, M. et al. 2005 in Scientific Detectors for Astronomy, eds. P. Amico & J. W. Beletic (Dordrecht: Springer), in press

Waczynski, A. et al. 2005, Proc. SPIE, 5902, 161